

## X-RAY SPECTRAL VARIATIONS IN THE YOUNGEST GALACTIC SUPERNOVA REMNANT G1.9+0.3

STEPHEN P. REYNOLDS,<sup>1</sup> KAZIMIERZ J. BORKOWSKI,<sup>1</sup> DAVID A. GREEN,<sup>2</sup> UNA HWANG,<sup>3</sup> ILANA HARRUS,<sup>3</sup> & ROBERT PETRE<sup>3</sup>*Accepted by ApJL*

## ABSTRACT

The discovery of the youngest Galactic supernova remnant (SNR) G1.9+0.3 has allowed a look at a stage of SNR evolution never before observed. We analyze the 50 ks *Chandra* observation with particular regard to spectral variations. The very high column density ( $N_H \sim 6 \times 10^{22} \text{ cm}^{-2}$ ) implies that dust scattering is important, and we use a simple scattering model in our spectral analysis. The integrated X-ray spectrum of G1.9+0.3 is well described by synchrotron emission from a power-law electron distribution with an exponential cutoff. Using our measured radio flux and including scattering effects, we find a rolloff frequency of  $5.4(3.0, 10.2) \times 10^{17} \text{ Hz}$  ( $h\nu_{\text{roll}} = 2.2 \text{ keV}$ ). Including scattering in a two-region model gives lower values of  $\nu_{\text{roll}}$  by over a factor of 2. Dividing G1.9+0.3 into six regions, we find a systematic pattern in which spectra are hardest (highest  $\nu_{\text{roll}}$ ) in the bright SE and NW limbs of the shell. They steepen as one moves around the shell or into the interior. The extensions beyond the bright parts of the shell have the hardest spectra of all. We interpret the results in terms of dependence of shock acceleration properties on the obliquity angle  $\theta_{\text{Bn}}$  between the shock velocity and a fairly uniform upstream magnetic field. This interpretation probably requires a Type Ia event. If electron acceleration is limited by synchrotron losses, the spectral variations require obliquity-dependence of the acceleration rate independent of the magnetic-field strength.

*Subject headings:* supernova remnants — ISM: individual (G1.9+0.3) — X-rays: ISM

## 1. INTRODUCTION

The supernova remnant (SNR) G1.9+0.3 has recently been shown to have expanded by about 16% between 1985 and 2007, implying an age of order 100 years – the youngest supernova remnant in the Galaxy (Reynolds et al. 2008, hereafter Paper I). The expansion was confirmed with new VLA observations from March 2008 (Green et al. 2008). The X-ray and current radio images are shown in Fig. 1. The X-ray spectrum is featureless and well described by the loss-steepened tail of the synchrotron spectrum inferred from radio frequencies. No thermal X-ray emission is apparent. G1.9+0.3 provides a unique opportunity to study a SNR at a stage never before observed, and to learn about the physics of shock acceleration in faster shocks than seen in any SNR ( $v_s \sim 14,000 \text{ km s}^{-1}$ ; Paper I).

A simple model of a power-law electron distribution with an exponential cutoff at energy  $E_{\text{max}}$  producing synchrotron radiation (XSPEC model `srcut`) has proved to be a useful tool in understanding X-ray synchrotron spectra in those dozen or so SNRs in which the phenomenon is observed (Reynolds 2008). The synchrotron spectrum cuts off more slowly than exponential, roughly as  $S_X \propto \exp[-(\nu/\nu_{\text{roll}})^{1/2}]$ . In addition to foreground absorption, this model requires three parameters: a 1 GHz radio flux  $S_9$ , a mean radio-to-X-ray spectral index  $\alpha$  ( $S_\nu \propto \nu^{-\alpha}$ ), and a rolloff frequency  $\nu_{\text{roll}}$ , the “critical frequency” for electrons with energy  $E_{\text{max}}$ , related to  $E_{\text{max}}$  by  $E_{\text{max}} = 39(h\nu_{\text{roll}}/1 \text{ keV})^{1/2}(B/10 \text{ } \mu\text{G})^{1/2} \text{ TeV}$ . In applying this model in Paper I, we used  $S_9 = 0.9 \text{ Jy}$ ,

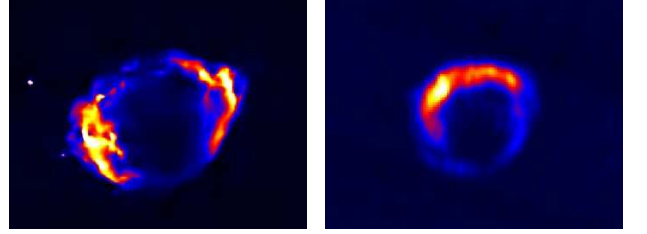


FIG. 1.— Left: *Chandra* image of G1.9+0.3, platelet smoothed (Willett 2007). Colors are intensities only, between 1.5 and 6 keV. Image size  $136'' \times 185''$ . Right: 2008 radio image of G1.9+0.3 (Green et al. 2008): VLA at 4.9 GHz. Resolution  $10'' \times 4''$ .

and obtained  $\nu_{\text{roll}} = 1.4 \times 10^{18} \text{ Hz}$ , but with a very high absorbing column density,  $N_H = (5.5 \pm 0.3) \times 10^{22} \text{ cm}^{-2}$ , implying significant scattering by dust along the line of sight. Such scattering removes photons from the source and distributes them in a faint halo out to arcminute distances, but can also redistribute photons across the source, in both cases in an energy-dependent fashion.

Below we present a reanalysis of the *Chandra* observation using Markov chain Monte Carlo (MCMC) techniques, including the effects of dust scattering, with an emphasis on characterizing spatial variations. Such variations hold important information on how the acceleration of electrons and/or magnetic-field amplification depends on different conditions such as shock speed and the obliquity angle  $\theta_{\text{Bn}}$  between the shock normal and upstream magnetic field, information crucial in understanding shock acceleration in different astrophysical environments.

## 2. SPECTRAL ANALYSIS METHODS

Radial averages of *Chandra* data show a dust-scattered halo out to about  $3'$ . Thus, the spectral analysis of

<sup>1</sup> Department of Physics, North Carolina State University, Raleigh NC 27695-8202; stephen\_reynolds@ncsu.edu

<sup>2</sup> Cavendish Laboratory; 19 J.J. Thomson Ave., Cambridge CB3 0HE, UK

<sup>3</sup> NASA/GSFC, Code 660, Greenbelt, MD 20771

G1.9+0.3 must be conducted jointly with a halo analysis. First, we refit the integrated spectrum without scattering, using a different abundance set for absorption (Grevesse & Sauval 1998), and a slightly different, improved background model. We then performed a joint analysis of the background-subtracted spectra from the source (innermost ellipse) and halo (between two outer ellipses) regions shown in Figure 2.

We consider a simple uniform dust distribution along the line of sight to G1.9+0.3, using total and differential X-ray scattering cross sections from Draine (2003). Small-angle scattering by dust out of the G1.9+0.3 source extraction region attenuates the X-ray spectrum by a factor of  $\exp(-\tau_{sca}) + f_{src}(1 - \exp(-\tau_{sca}))$ , where  $\tau_{sca}$  is the energy-dependent optical depth for scattering, and  $f_{src}$  is the energy-dependent fraction of photons that have been scattered into the source extraction region. Unless there are large quantities of dust in the immediate vicinity of the SNR, it is sufficient to consider only singly scattered photons in the second term containing  $f_{src}$ . The fraction of singly scattered photons is equal to  $\tau_{sca} \exp(-\tau_{sca})$  (e.g., Mathis & Lee 1991), so scattering attenuates the source spectrum by  $(1 + f_{src}\tau_{sca}) \exp(-\tau_{sca})$ . The fraction  $f_{src}$  depends on the assumed dust distribution and the spatial structure of the X-ray emitting gas. For a point source, the angular distribution of singly-scattered photons can be readily found from eq. (19) of Draine (2003). We approximated the spatial structure of G1.9+0.3 by the platelet-smoothed (Willett 2007) image shown in Figure 1, and convolved it with the model point source halo to arrive at  $f_{src}$ . Similarly, the halo region flux is proportional to  $f_{halo}(1 - \exp(-\tau_{sca}))$ , or  $f_{halo}\tau_{sca} \exp(-\tau_{sca})$  for singly scattered photons. We neglect multiply scattered photons in modeling of the G1.9+0.3 dust halo – this underpredicts the halo intensity at low energies where  $\tau_{sca}$  exceeds unity, by at most 30% and probably less (Smith et al. 2006). We investigated the effect of the *Chandra* point-spread function (PSF), but found that only about 1% of the SNR flux at high energies is scattered within the telescope into the halo extraction annulus.

We performed joint modeling of the G1.9+0.3 and halo spectra within the XSPEC software package (Arnaud 1996), with dust scattering and PSF effects implemented as local multiplicative models. Model input parameters are energy-dependent functions  $f_{psf}$  (the energy-dependent fraction of the SNR flux scattered into the halo extraction region),  $f_{src}$ , and  $f_{halo}$ , and a scalar parameter  $N_H^{sca}$  that provides scaling for  $\tau_{sca}$  in terms of the effective H column density for dust scattering. Under a single-scattering approximation,  $f_{src}$  and  $f_{halo}$  depend only on the dust distribution along the line of sight, not on  $\tau_{sca}$ , so they may be specified prior to modeling spectra. We use the `srcut` model described above for the intrinsic X-ray spectrum. While background subtracted spectra are shown for clarity in Figure 2, we do not subtract background prior to modeling so that we may use MCMC methods as implemented in XSPEC and PyMC<sup>4</sup>. We determined the normalization parameter  $S_9$  from our 1.5 GHz radio image, extrapolated to 1 GHz

using a spectral index of 0.62 (Green et al. 2008), obtaining a value of 1.17 Jy (under the possibly incorrect assumption that all the radio flux comes from the same population of electrons as produces the X-rays). The absorbing and scattering column densities may differ if any of the assumptions underlying our uniform-dust model break down, e.g., an excess of dust local to the SNR will not affect absorption but will reduce large-angle scattering, resulting in  $N_H > N_H^{sca}$ .

It is important to model the background correctly in view of the faintness of the dust scattered halo. We extracted a background spectrum from a large ( $7.6' \times 3.2'$  in size) region on the ACIS S3 chip beyond the dust-scattered halo. To separate sky and particle backgrounds, we also extracted spectra from the most recent stowed (particle only) ACIS S3 background file available online at the CXC<sup>5</sup>. This particle-only spectrum was fit with a combination of Gaussians and power laws, exponentially cut off on both ends. We then modeled our background spectrum as a combination of a sky background, consisting of two absorbed power laws, and a particle-only background (allowing for change in intensity only). This fit, after appropriate scaling and again allowing for variations in the particle background intensity, was used in the modeling reported below.

The Bayesian MCMC methods require specification of priors on unknown (fitted) parameters. Uniform, non-informative priors were used for  $N_H$ ,  $N_H^{sca}$ ,  $\alpha$ ,  $\log \nu_{roll}$ ,  $\Gamma$ , and  $\log F_X$ , with the following exceptions. In the spatially-resolved five-region analysis, we employed a normal prior for  $\alpha$  with the measured radio index of 0.62 and estimated standard (1  $\sigma$ ) error of 0.02. A normal prior for  $N_H$  was assumed for protruding SE and NW extensions (“ears”), based on results of that fit. Since results are prior-dependent in this case, we also imposed an upper cutoff of  $\nu_{roll} = 10^{21}$  Hz on the corresponding prior, as theoretical considerations make higher rolloff frequencies unlikely.

### 3. MODELING AND RESULTS

We quantified the azimuthal brightness variations obvious in Figure 1 by circumscribing the shell with an elliptical annulus of width  $19''$ , and dividing it into 18 equal segments. We found about a factor of 6 variation between the bright NW and SE limbs and the fainter regions between.

Table 1 shows results for modeling the integrated spectrum with the `srcut` model. Column 1 shows the improved no-scattering parameter values (means derived from MCMC chains) and their 5 and 95 percentile scores. Column 2 shows the corresponding values with our simple scattering model. The chief difference is a lowering of  $\nu_{roll}$  by about 50%. The new value,  $5.4 \times 10^{17}$  Hz ( $h\nu_{roll} = 2.2$  keV) is still among the highest for a shell SNR. In the third and fourth columns we give results from a two-zone model, with the zones comprising most of the bright emission from the SE and NW limbs, in addition to a halo. Absorptions were tied together for the two regions, while the contribution from scattering from the “missing” faint limbs and center was accounted for by artificially increasing scattering by 20%, required to obtain consistency in the derived  $N_H$  values with the

<sup>4</sup> Patil, Huard, & Fonnesbeck (2009) PyMC: Markov chain Monte Carlo for Python, version 2.0. Available at <http://pymc.googlecode.com>.

<sup>5</sup> <http://cxc.harvard.edu/contrib/maxim/acisbg>

value from the spatially-integrated model. The spectral indices  $\alpha$  differ at the 99.98% level, and  $\nu_{\text{roll}}$  values at the 94% level. A similar simulation neglecting dust scattering gave qualitatively similar results but higher  $\nu_{\text{roll}}$  values by over a factor of 2, indicating the importance of including dust scattering. These regions include about 80% of the X-ray counts, but less than half the radio, suggesting that some of the radio flux may not be associated with the blast wave.

Spectral results at higher angular resolution are desirable. We subdivided G1.9+0.3 into six regions as shown in Figure 2, but the X-ray data were not adequate to permit the use of the scattering model. Since scattering moves photons both out of the source and from brighter regions into fainter ones, the predominant effect is to smooth gradients, in both total brightness and spectrum, so these results should underestimate the true spatial variations. For a model-independent description of the observed data, we described the six regions simultaneously with power laws, tying the absorption columns together, but we also performed **srcut** modeling. Here the clearly discrepant radio properties of the “ears” made it necessary to impose a different prior on  $\alpha$  (flat) than for the five regions within the source ellipse, so the “ears” modeling was performed separately. We also bounded the flat prior on  $\log \nu_{\text{roll}}$  by  $\log \nu_{\text{roll}}(\text{max}) = 21.0$ . Table 2 gives both power-law photon indices  $\Gamma$  ( $N(h\nu) \propto (h\nu)^{-\Gamma}$  ph cm $^{-2}$  s $^{-1}$ ) and **srcut** parameters.

The systematic trends with brightness are apparent: the opposing bright limbs of the shell have harder spectra (either lower  $\Gamma$  or higher  $\nu_{\text{roll}}$ ) than the center, and the spectra soften also moving to the interior. The projecting fainter “ears” beyond the E and W peaks were combined for better statistics, and have the flattest spectra of all. The correlation of X-ray brightness with  $\nu_{\text{roll}}$  strongly suggests a single cause. Our primary observational result is this systematic variation of spectral hardness, correlated with brightness. A complete dust-scattering model, including the effects of scattering back into source regions, applied to the spatially resolved data will require better X-ray data, but while the numerical values for  $\nu_{\text{roll}}$  will change somewhat, we do not expect these trends to be reversed.

#### 4. DISCUSSION

We summarize our results as follows:

1. Including dust scattering lowers  $\nu_{\text{roll}}$  by about 50% in the integrated spectrum, and by factors of more than 2 in the two-region fit, significantly lowering the inferred maximum electron energies. However, the  $\nu_{\text{roll}}$  values are still among the highest ever reported. The mean spectrum between radio and X-rays is significantly flatter in the SE than in radio alone for our two-zone model.
2. Both X-ray brightness and spectral flatness or  $\nu_{\text{roll}}$  show strong bilateral symmetry. As one moves away from the bright SE and NW limbs in azimuth or toward the center, the mean surface brightness drops by at least 6, while values of  $\nu_{\text{roll}}$  drop by about an order of magnitude.
3. The radio structure is dominated by a bright shell

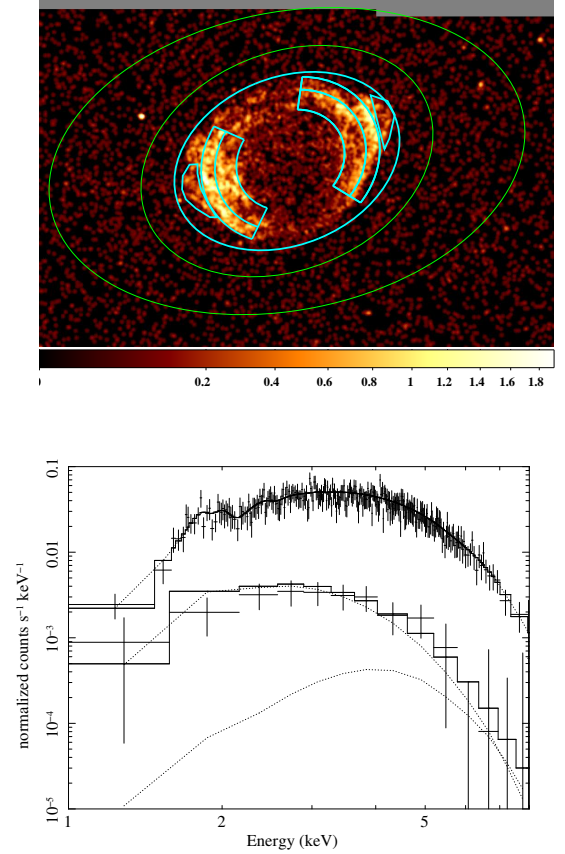


FIG. 2.— Top: Raw *Chandra* image of G1.9+0.3, showing source (cyan) and background (green) regions. The six regions used for spatially-resolved modeling are indicated (the “ears” are the sum of the two irregular regions, and the faint limbs and center comprise the remainder of the source). Colors are intensities only (ct pixel $^{-1}$ ), between 1.5 and 6 keV. The image has been smoothed with a Gaussian with  $\sigma = 3$  pixels (1.5”). Bottom: Integrated spectrum of G1.9+0.3 and of its halo (top and bottom, respectively), extracted from regions shown above, after background subtraction and adaptive binning (both done for display purposes only). Model: **srcut** modified by scattering (see text). For the halo spectrum, contributions from scattering by dust and within the telescope are shown separately (upper and lower dotted curves, respectively). Two point sources within the dust-scattering halo region (between outermost two ellipses) were excluded.

with somewhat smaller peak radius than the X-ray shell, and a single intensity maximum.

4. The “ears” extending beyond the SE and NW rims in X-rays show the hardest spectra of all, and are not detected at radio wavelengths.

The relatively poor correlation of radio and X-ray brightness around the shell, and the smaller radius of the peak of the radio shell, suggest that much of the radio emission may not originate at the outer blast wave, but further inside, perhaps due to electron acceleration and/or turbulent magnetic-field amplification at the contact discontinuity between shocked ISM and shocked ejecta, as is probably the case in Cas A (e.g., Cowsik & Sarkar 1984). We focus on the X-ray structure and spectra.

In principle, the systematic azimuthal brightness variations could be due to an inhomogeneous upstream medium that has the bilateral symmetry of G1.9+0.3. This explanation requires higher densities in the SE and NW, where they would be expected to impede the expansion. However, the remnant has a larger SE-NW than NE-SW diameter. It is equally unlikely to imagine systematically larger magnetic fields on opposite sides of the remnant. However, the observed simple bilateral symmetry of both brightness and spectral variations can arise naturally if electron injection, acceleration rate, or magnetic-field amplification depend somehow on shock obliquity  $\theta_{\text{Bn}}$ . (The physical origin of such dependences is not clear.) If the magnetic field is roughly uniform and not too far from the plane of the sky, then as a spherical shock encounters it, the obliquity angle around the remnant periphery will vary with the observed bilateral symmetry. That explanation essentially requires the supernova to be Type Ia, as a core-collapse supernova is expected to expand into stellar-wind material with a frozen-in magnetic field in a tightly wound Parker spiral (roughly azimuthally oriented) with all obliquities therefore near  $90^\circ$ .

Synchrotron brightness from a power-law distribution of electrons  $N(E) = KE^{-(2\alpha+1)}$  varies as  $KB^{1+\alpha}$ . The electron energy density can vary with obliquity if the injection or acceleration rate depends on  $\theta_{\text{Bn}}$ , while the magnetic-field strength will vary due to simple flux-freezing and shock compression of the tangential component, and possibly also to turbulent amplification due to cosmic-ray-induced instabilities (e.g., Bell & Lucek 2001), a process which might also have obliquity dependence. However, in all known cases, X-ray synchrotron emission is produced by electrons on the loss-steepened tail of a power-law distribution (e.g., Reynolds & Keohane 1999), introducing a third parameter. For the simple **srcut** model, that parameter is the rolloff frequency  $\nu_{\text{roll}}$ . X-ray brightness will vary even for constant  $K$  and  $B$  if  $\nu_{\text{roll}}$  varies, and brighter regions will have harder spectra.

For a uniform upstream magnetic field, if the post-shock field is simply compressed, a strong-shock compression ratio of 4 will produce post-shock magnetic fields four times larger where the shock is perpendicular ( $\theta_{\text{Bn}} \sim 90^\circ$ ), and hence a larger synchrotron emissivity by  $4^{1+\alpha} = 9.5$  compared to where  $\theta_{\text{Bn}} \sim 0^\circ$  (using  $\alpha = 0.62$ ; Green et al. 2008). This is adequate to explain the required factor of about 6, but would imply that the bright limbs are projections of an equatorial “belt” which might be detectable across the remnant center in a deeper observation.

Standard first-order Fermi shock acceleration in the test-particle limit predicts a spectral index  $\alpha = 0.5$  for a strong shock. Steeper radio indices are universal in young remnants, perhaps indicating cosmic-ray-modified shocks (e.g., Reynolds & Ellison 1992). We find a steeper radio-to-X-ray value of  $\alpha$  than that in the radio alone, consistent with the expectation of modified shocks. Better radio data will be required to confirm the radio index and search for possible spatial variations.

In Fermi shock acceleration, three possible limitations on  $E_{\text{max}}$  are synchrotron losses ( $E_{m1}$ ), finite age (or size;  $E_{m2}$ ), and escape due to an abrupt change in upstream

diffusion properties ( $E_{m3}$ ) (Reynolds 1998). These depend differently on physical parameters, including shock obliquity, which may affect the acceleration rates (Jokipii 1987). If we lump all such obliquity dependence into a factor  $f_{\text{tbn}}(\theta_{\text{Bn}})$ , the corresponding rolloff frequencies obey  $\nu_{\text{roll}} \propto E_{\text{max}}^2 B$  and we have

$$\nu_{m1} \propto f_{\text{tbn}} u_8^2 \quad \nu_{m2} \propto f_{\text{tbn}}^2 B_2^3 t^2 u_8^4 \quad \nu_{m3} \propto \lambda_m^3 B_1^2 B_2 \quad (1)$$

where  $B_1$  and  $B_2$  are the upstream and downstream magnetic-field strengths, respectively,  $u_8 \equiv u_{\text{sh}}/10^8 \text{ cm s}^{-1}$ , and  $\lambda_m$  is a wavelength of MHD waves above which the diffusion coefficient is assumed to jump to much larger values, mimicking the absence of longer waves capable of scattering more energetic particles.

The absence of  $B$ -dependence in  $\nu_{m1}$  means that if electron energies are limited by radiative losses, the different spectral slopes cannot be produced purely by varying the magnetic field. The strong shock-speed dependence could produce a significant effect; but the observed order-of-magnitude variation in  $\nu_{\text{roll}}$  would require a greater variation in  $u_{\text{sh}}$  than seems consistent with the remnant’s circular outline to within about 10%.

Since  $B_2/B_1$  is obliquity-dependent, either age-limited (case 2) or escape-limited (case 3) acceleration can explain some spectral variations with obliquity even if  $f_{\text{tbn}} \equiv 1$ . A non-linear variant of escape-limited acceleration in which  $\lambda_m$  grows as increasingly higher-energy particles escape might be able to provide the observed range; otherwise one expects  $\lambda_m$  roughly constant, a property of the upstream medium, giving a maximum variation of  $\nu_{m3}$  of 4 or so. Age-limited acceleration could easily accomplish this without additional obliquity-dependence, since  $B_2^3$  will vary by a factor of at least 64. We conclude that a minimal explanation of both brightness and spectral variations is interaction of the blast wave with a roughly uniform magnetic field parallel to the bright rims (roughly SW – NE), with no additional obliquity-dependence of either electron injection or of acceleration rates. In that case, the “ears” must represent enhanced upstream diffusion where the shock is perpendicular, which seems unlikely since cross-field diffusion mean free paths are probably limited to the gyroradius. However, a preshock-diffusion explanation is consistent with the lack of radio emission from the “ears” (as lower-energy radio-emitting electrons would not diffuse as far ahead of the shock). In this case, an **srcut** model for the “ears” would not be appropriate, as already suggested by their discrepant value of  $\alpha$ .

An alternative explanation involves a magnetic field in which the shock is parallel at the “ears.” This would almost certainly require enough turbulent amplification of magnetic field to swamp the frozen-in field increase where the shock is perpendicular. In addition, the magnetic field would need to be quite close to the plane of the sky, so that the bright limbs, now “polar caps” seen edge-on, are at the edge of the remnant in projection. The same requirement occurs for this geometry in SN 1006. Strong magnetic-field amplification probably requires efficient shock acceleration, so that a population of energetic ions is implied. However, for any magnetic-field geometry, effects due solely to magnetic-field dependence of acceleration time cannot produce the spectral variations if electron acceleration is limited by synchrotron

TABLE 1  
SPECTRAL FITS

Region	Whole (no scat)	Whole (scat)	SE	Two regions (scat)	NW
$N_H$ (abs) ( $\times 10^{22}$ cm $^{-2}$ )	6.76 (6.37, 7.16)	5.06 (4.48, 5.62)		5.12 (4.56, 5.68)	
$N_H$ (scat)		3.48 (2.68, 4.35)		3.60 (2.83, 4.41)	
$S_9$ (Jy)	1.17	1.17	0.203		0.291
$\alpha$	0.649 (0.625, 0.673)	0.634 (0.614, 0.655)	0.566 (0.541, 0.592)		0.612 (0.588, 0.637)
$\log \nu_{\text{roll}}$ (Hz)	17.90 (17.58, 18.29)	17.73 (17.48, 18.01)	17.48 (17.23, 17.76)		17.72 (17.44, 18.06)

NOTE. — Errors are 90% confidence limits throughout. The no-scattering fit updates the values from Paper I.

TABLE 2  
MULTI-REGION SPECTRAL PARAMETERS

Region	$S_9$ (mJy)	$\alpha$	$\log \nu_{\text{roll}}$ (Hz)	$\Gamma$	Flux
Outer SE	67	$0.60 \pm 0.02$	18.12 (17.80, 18.52)	2.2 (2.1, 2.4)	6.5 (6.2, 6.9)
Inner SE	190	$0.62 \pm 0.02$	17.46 (17.24, 17.70)	2.6 (2.4, 2.8)	4.4 (4.2, 4.7)
Faint limbs, center	600	$0.63 \pm 0.02$	17.16 (16.98, 17.35)	2.8 (2.6, 3.0)	5.8 (5.4, 6.2)
Outer NW	68	$0.63 \pm 0.02$	18.55 (18.06, 19.21)	2.1 (1.9, 2.3)	4.8 (4.5, 5.1)
Inner NW	220	$0.64 \pm 0.03$	17.69 (17.43, 18.00)	2.4 (2.2, 2.6)	4.7 (4.4, 5.0)
“Ears”	< 2	< $0.51 \pm 0.04$	< 18.67 (17.65, 20.37)	2.0 (1.7, 2.2)	3.4 (3.1, 3.7)

NOTE. — Errors are 90% confidence limits. Fitted absorption  $N_H = 7.3$  (6.8, 7.7)  $\times 10^{22}$  cm $^{-2}$  for power-law models and 6.9 (6.6, 7.1)  $\times 10^{22}$  cm $^{-2}$  for *srcut* models. Flux is in units of  $10^{-13}$  ergs cm $^{-2}$  s $^{-1}$  between 1 and 8 keV. “Ears” *srcut* modeling was performed independently: we assumed a flat prior on  $\nu_{\text{roll}}$  to a maximum  $\log \nu_{\text{roll}} = 21.0$ , and a flat prior on  $\alpha$ .

losses.

Currently scheduled observations may allow considerable clarification. Our 250-ks *Chandra* follow-up, and the higher-resolution VLA study we have undertaken, should allow better understanding of the relation of radio to X-ray electron populations, better characterization of the scattering, and better deduction of spatially resolved

spectral properties. G1.9+0.3 will provide valuable constraints on the obliquity-dependence of shock acceleration and magnetic-field amplification.

This work was supported by NASA through Chandra General Observer Program grant GO6-7059X.

## REFERENCES

- Arnaud, K.A. 1996, in *Astronomical Data Analysis Software and Systems V*, eds. G. Jacoby & J. Barnes ASP Conf. Ser. 101, 17  
 Bell, A.R., & Lucek, S.G. 2001, *MNRAS*, 321, 433  
 Cowsik, R., & Sarkar, S. 1984, *MNRAS*, 207, 745  
 Draine, B. T. 2003, *ApJ*, 598, 1026  
 Green, D.A., et al. 2008, *MNRAS*, 387, L54  
 Grevesse, N., & Sauval, A. J. 1998, *Space Science Reviews*, 85, 161  
 Jokipii, J.R. 1987, *ApJ*, 313, 842  
 Mathis, J. S., & Lee, C. W. 1991, *ApJ*, 376, 490  
 Reynolds, S.P. 1998, *ApJ*, 493, 375 (R98)  
 Reynolds, S.P. 2008, *ARA&A*, 46, 89  
 Reynolds, S.P., et al. 2008, *ApJ*, 680, L41 (Paper I)  
 Reynolds, S.P., & Ellison, D.C. 1992, *ApJ*, 399, L75  
 Reynolds, S.P., & Keohane, J.W. 1999, *ApJ*, 525, 368  
 Smith, R.K., et al. 2006, *ApJ*, 648, 452  
 Willett, R. 2007, in *Statistical Challenges in Modern Astronomy IV*, eds. G.J. Babu & E.D. Feigelson, APS Conf. Ser. 371, 247